Geophysical Journal International

Geophys. J. Int. (2014) **198,** 880–894 doi: 10.1093/gji/ggu166

GJI Marine geosciences and applied geophysics

High definition cross-well electrical resistivity imaging using seismoelectric focusing and image-guided inversion

P. Sava,[1] A. Revil[1,2] and M. Karaoulis[1]

[1] *Colorado School of Mines, Department of Geophysics, Golden, CO, USA*

[2] *ISTerre, CNRS, UMR CNRS* 5275, *Université de Savoie, F-*73376, *Le Bourget du Lac Cedex, France. E-mail: arevil@mines.edu*

Accepted 2014 May 6. Received 2014 March 10; in original form 2014 January 2

SUMMARY

We propose a new, simple and efficient method to image electrical resistivity between a set of wells. Our procedure consists of two steps: first, we map the interfaces between various subsurface formations using seismoelectric conversions; second, we derive the formation resistivity using image-guided cross-well electric tomography. In the first step, we focus seismic energy at a set of points located on a regular grid between wells, which enables us to map the geological formations in terms of heterogeneities in electrical, hydraulic and/or seismic properties. The density of the scanning points (i.e. the seismoelectric image resolution) is related to the wavelength of the seismic impulse used to scan the formations. Each time the seismic energy is focused at a point, the resulting electrical potential burst (equivalent to the one generated by a volumetric seismic source) is recorded remotely at a set of electrodes positioned in wells (the reference electrode can be located on the ground surface or far enough to be considered at infinity). We construct a high-resolution 'seismoelectric' image by assigning the electrical potential simulated at these fixed electrodes to the location of the seismic focus. In a follow-up step, the structure of this image is used in image-guided inversion to improve electrical resistivity tomography between the two wells. The structural information from the seismoelectric image is used to impose constraints on the model covariance matrix used in the inversion of the electrical resistivity data. This approach offers new perspectives in recovering fine structure of resistivity (high definition resistivity tomography) between the wells, which cannot be resolved through conventional cross-well resistivity or from seismic tomography alone.

Key words: Image processing; Tomography; Electromagnetic theory; Magnetic and electrical properties; Hydrogeophysics.

1 INTRODUCTION

Sava & Revil (2012) and Revil *et al.* (2014) have recently proposed a new geophysical method combining the advantage of electrical and seismic methods (sensitivity to fluid contents and resolution). This method, to which we refer as SeismoElectric Focusing, consists of concentrating seismic waves at a collection of scanning points and measuring remotely the resulting electrical field. The conversion between the hydromechanical energy and the electromagnetic energy is electrokinetic in nature, and thus it is related to the relative displacement between the charged pore water and the charged grains (Frenkel 1944). The charging mechanism is related to the existence of the electrical double layer coating the surface of the solid phase in contact with the pore water (Davis *et al.* 1978; Revil & Mahardika 2013). This electrical double layer is responsible for an excess of electrical charge in the pore space and the drag of this excess electrical charge associated with the poroelastic deformation of the material is responsible for an electrical current density of electrokinetic nature (Pride 1994). In the presence of a concentrated hydromechanical disturbance (e.g. associated with the focusing of a seismic wave), we have an associated burst in the electrical field as explained numerically and experimentally by Mahardika *et al.* (2012) and Haas *et al.* (2013), respectively. Various studies have demonstrated that these seismoelectric signals are characterized by signal-to-noise ratio high enough to be measured in the laboratory (e.g. Zhu *et al.* 1999; Zhu & Toksöz 2003) and in the field (e.g. Butler 1996; Garambois & Dietrich 2001; Dupuis & Butler 2006; Kulessa *et al.* 2006; Dupuis *et al.* 2007, 2009).

Our goal is to improve the resolution of resistivity and complex resistivity tomograms. Techniques have been recently developed to incorporate structural information in these tomograms (e.g. Zhou *et al.* 2014). The advantages of getting better resistivity or complex resistivity distribution (over space and time), is to apply recently developed petrophysical transforms to these

© The Authors 2014. Published by Oxford University Press on behalf of The Royal Astronomical Society.

Downloaded from http://gji.oxfordjournals.org/ at Colorado School of Mines on June 26, 2014

tomograms to recover permeability and saturation. For example, Revil (2012, 2013a,b) have developed a set of petrophysical models to complex electrical conductivity that could be used to determine permeability (inside one order of magnitude) from complex conductivity data performed in a range of frequencies (see also Kemna 2000).

The idea promoted by Sava & Revil (2012) is to develop virtual current electrodes at any position of a geological formation in order to improve resistivity tomography. In this paper, we keep the basic idea of Sava & Revil (2012) based on seismic focusing, and develop a simple yet efficient technique to produce an electrical potential map revealing the position of heterogeneities at every location in space. This map is subsequently used to modify the model covariance matrix in resistivity tomography in order to incorporate this structural information into the cross-well electrical resistivity problem. This procedure is demonstrated in this paper for the case of a synthetic earth model between two wells. In this synthetic study, the final resistivity image is significantly improved (both in terms of structure and resistivity values) in comparison with a classical cross-well electrical resistivity tomography using conventional Tikhonov regularization with isotropic smoothness (Loke & Barker 1995; Loke & Lane 2002; Günther *et al.* 2006). The image guided inversion procedure is similar with the one employed by Hale (2009a,b,c) for interpolation of elastic parameters with guidance from a seismic (migrated) section, or by Zhou *et al.* (2014) for constraining electrical tomography using GPR data or geological information.

2 METHODOLOGY

2.1 Streaming current density

An electrical current, called the streaming electrical current, is associated with the drag of the diffuse layer with respect to the elastic skeleton of a porous material by the flow of the pore water. The diffuse layer is part of the electrical double layer coating the surface of the grains (Fig. 1a). The existence of the electrical diffuse layer implies that a fraction of the countercharge (balancing the charge on the mineral surface) is mobile and can be therefore displaced by the flow of the pore water (Fig. 1b).

The macroscopic source current density $\mathbf{J}_S$ (called the streaming current density, in A m^{-2}) can be obtained by taking the volume average of the local current density defined with respect to the deformation of the solid phase. Its expression is give by:

$$\mathbf{J}_S = \hat{Q}_V \dot{\mathbf{w}}, \tag{6}$$

where $\dot{\mathbf{w}}$ denotes the Darcy velocity (flux of water in a Lagrangian framework attached to the grains expressed in m s^{-1}) and $\hat{Q}_V$ denotes an effective charge density carried by the flow of the pore

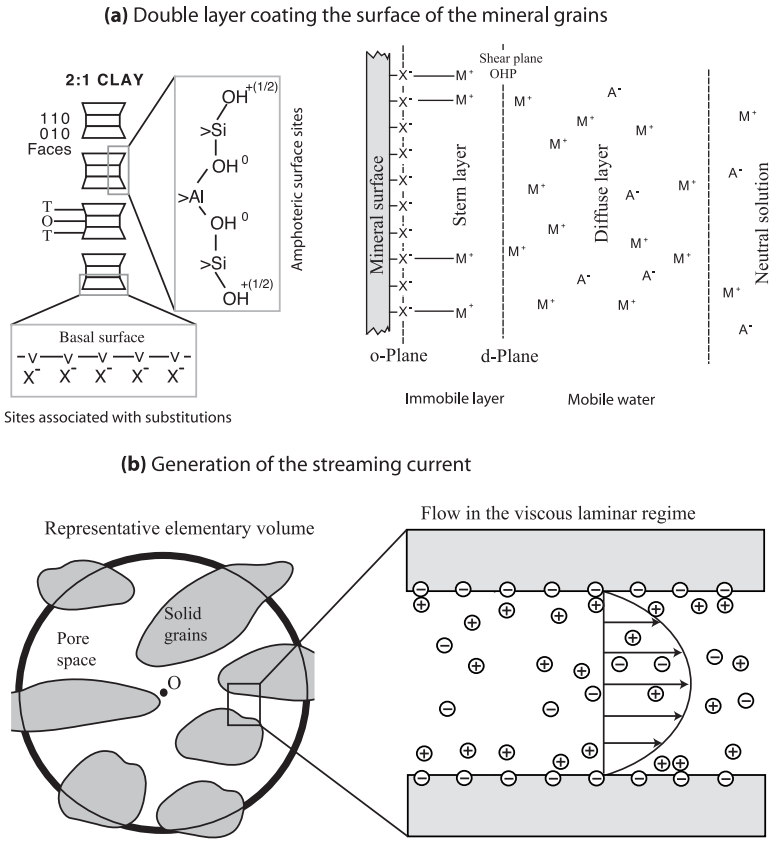


Figure 1. Influence of the electrical double layer on the generation of a streaming current. (a) An electrical double layer coats the surface of minerals (M^+ denotes the metal cation and A^- the anion). It is formed by a Stern layer of counterions sorbed on the mineral surface and a diffuse layer of mobile ions (see Stern 1924; Davis *et al.* 1978; Leroy & Revil 2004, 2009; Leroy *et al.* 2008). The charge that is not compensated in the Stern layer is compensated in the Gouy–Chapman diffuse layer (Gouy 1910; Chapman 1913). The charge density in these two layers counterbalances the charge density on the mineral surface (located on the o-plane). The shear plane (d-plane) defined the surface on which the relative velocity between the solid and fluid phases is null. (b) The flow of the pore water through each representative elementary volume of a porous material is responsible for a current density (the streaming current) associated with the drag of the excess of charge contained in the pore water.

Downloaded from http://gji.oxfordjournals.org/ at Colorado School of Mines on June 26, 2014

water. This effective charge density is sensitive to the permeability of the porous material (Revil & Mahardika 2013). According to Jardani *et al.* (2007) and Revil & Mahardika (2013), $\hat{Q}_V$ can be estimated from the permeability k (m^2) by:

$$\log_{10} \hat{Q}_V = -9.23 - 0.82 \log_{10} k. \quad (7)$$

This seismoelectric theory is an extension of the streaming current theory to the propagation of seismic waves through porous media (Pride 1994). In Appendix A, we discuss the potential frequency dependence of the electrokinetic properties.

2.2 Poroacoustic wave modelling

Modelling seismoelectric conversion begins with seismic wave simulation in porous media (Pride 1994; Jardani *et al.* 2010). However, even the Biot dynamic poroelasticity fails to predict accurately the amplitude of the seismic waves as various low-frequency attenuation mechanisms (like squirt-flow mechanisms) are not taking into account in this theory. Sava & Revil (2012) and recently Revil *et al.* (2014) propose to use the acoustic approximation and develop a simpler electrokinetic theory to model seismoelectric signals, but that present the clear advantages to be easily extendable to unsaturated and two phase flow conditions (e.g. Revil and Mahardika 2013; Revil *et al.* 2014, and references therein). We note that this model produces seismoelectric amplitudes that are comparable to the ones produced by the poroelastic approximations, although we do not concentrate on seismoelectric amplitudes in this paper. Here, we only require that seismoelectric signals have amplitudes that are above the noise level so they can be properly recorded in field conditions.

Our numerical model relies on solving the acoustic wave equation,

$$\frac{\partial^2 P}{\partial t^2} - \left(K_u + \frac{4}{3}G\right) \nabla \cdot \left(\frac{1}{\rho} \nabla P\right) = f(\mathbf{x}, t), \quad (8)$$

where P denotes the confining pressure, ρ the mass density of the material in kg m^{-3}, K_u the bulk modulus (in Pa) in undrained conditions, G describes the shear modulus of the skeleton (frame) of the porous material and $f(\mathbf{x}, t)$ denotes the source function at position $\mathbf{x}$ and time t. The seismic source $f(\mathbf{x}, t)$ is described in Sava & Revil (2012). Despite the fact that we use a pulse-like source function in this paper (namely a Ricker wavelet), our approach could be also used with harmonic sources and we could potentially vibrate any point of a reservoir in a range of frequencies. This spectroscopic approach could be used to investigate resonance effects associated with fractures as recently discussed for instance by Jougnot *et al.* (2013) or with non-viscous fluid (see for instance Revil & Jardani 2010, who used viscoelastic fluids corresponding to the properties of heavy oils).

Much progress has been done recently in understanding the seismoelectric coupling in saturated and unsaturated porous media (Revil & Mahardika 2013). The seismoelectric coupling used below is however a simplified version of these theories (see Revil *et al.* 2014); we use the set of equations given in Sava & Revil (2012) for computational efficiency. The assumptions of this model are the following: (1) the frequency of interest is below the Biot frequency of relaxation (typically around 10 kHz) and squirt-flow mechanisms are neglected. (2) The use of the acoustic approximation implies that there are no shear waves and therefore no seismoelectric effects associated with the existence of shear waves. (3) The pore fluid pressure is related to the macroscopic pressure P (positive in compression) through the use of the Skempton coefficient B. (4) The

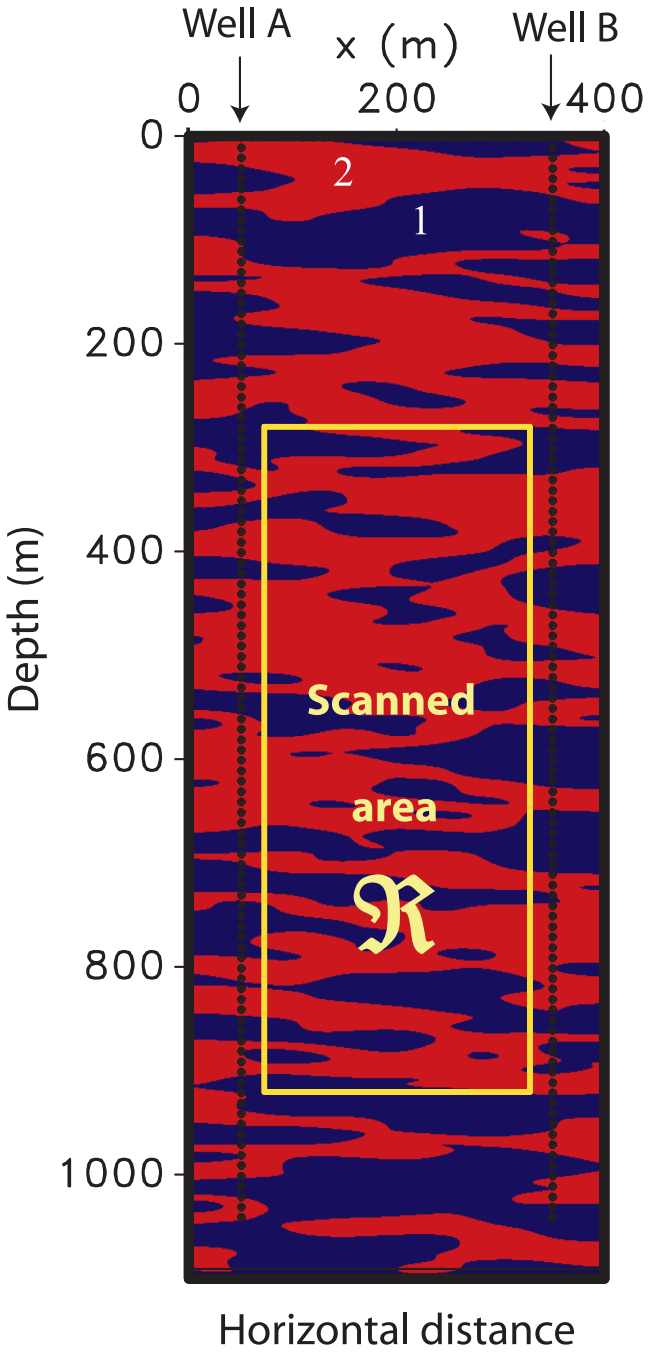


Figure 2. Model used for the simulations and geometry of the acquisition array. The porous material is bimodal with a larger correlation length in the horizontal direction. The seismic receivers are located in two wells (A and B). The area scanned through focusing is indicated by the yellow rectangle (scanning region $\Re$).

frequency dependence of the material properties are neglected. This is actually not a bad approximation as the frequency dependence of the electrical conductivity is weak (Vinegar & Waxman 1984; Revil 2012, 2013a,b) and below 1 kHz, the electrokinetic coupling does not depend on frequency (Revil & Mahardika 2013; Zhu & Toksöz 2013). The theoretical model used in this paper can easily be expanded to any frequency up to the MHz range by adding (1) the α-polarization of the electrical double layer, (2) the β-polarization (also called interfacial polarization or Maxwell Wagner polarization) and (3) the transition between viscous to inertial flow effects

Downloaded from http://gji.oxfordjournals.org/ at Colorado School of Mines on June 26, 2014

Table 1. Material properties used for the simulations. The viscosity of the pore water is taken equal to 10^{-3} Pa s and its bulk density equal to 1000 kg m^{-3}.

Property	Formation 1	Formation 2
Bulk modulus K_u (Pa)	22×10^9	7×10^9
Skempton coefficient B (−)	0.65	0.85
Density ρ (kg m^{-3})	2300	1900
Log (water phase permeability, k, m^2)	−12	−16
Electrical conductivity, σ (S m^{-1})	1.00	0.25
Bulk density, ρ (kg m^{-3})	1900	2300

(discussed in Appendix A). This type of model has already been developed in Revil (2013a,b) and Revil & Mahardika (2013).

In the model of Sava & Revil (2012), the fluctuations of the pressure P are responsible for fluctuations of the electrical potential ψ according to the following elliptic equation:

$$\nabla \cdot (\sigma \nabla \psi) = -\nabla \cdot \left[\frac{\hat{Q}_V k}{\eta_f} \nabla (BP) \right]. \tag{10}$$

Eq. (10) corrects a typo (about the sign) in eq. (12) of Sava & Revil (2012). In eq. (10), σ denotes the electrical conductivity of the material, k is the permeability (in m^2), η_f denotes the dynamic viscosity of the pore water (in Pa s) and B denotes the Skempton coefficient (Wang 2000). The question of the frequency dependence of the streaming potential coupling coefficient $C = -\hat{Q}_V k/(\eta_f \sigma)$ is discussed in Appendix A. We can safely neglect this frequency dependence for our study. Indeed, we consider that we are working in a frequency range below the transition between the viscous-laminar to inertial laminar flow regimes.

2.3 Petrophysics

Three material properties are needed for the hydromechanical equations: the mass density of the porous material ρ, the undrained bulk modulus K_u and the Skempton coefficient B. These properties are related to the pore fluid (index f) and solid (index s) by (e.g. Wang 2000),

$$\rho = (1-\phi)\rho_s + \phi \rho_f, \tag{11}$$

$$K_u = \frac{K_f (K_s - K) + \phi K \left(K_s - K_f\right)}{K_f (1 - \phi - K/K_s) + \phi K_s}, \tag{12}$$

$$B = \frac{1 - K/K_u}{1 - K/K_s}, \tag{13}$$

where ρ_s and ρ_f denote the mass density of the fluid and solid phases, K is the bulk modulus of the material (in Pa) also called the frame or skeleton bulk modulus (porous material without fluid) and K_f and K_S the bulk moduli of the fluid and solid phases (in Pa), respectively.

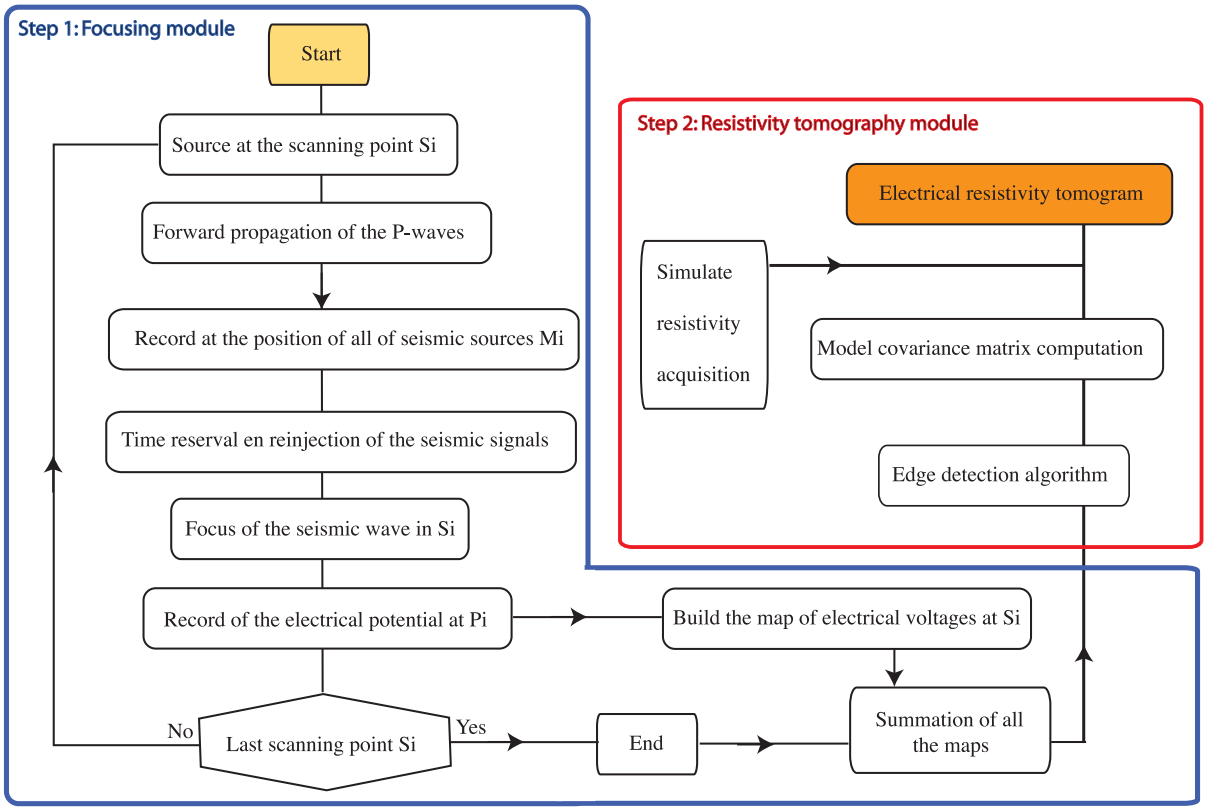


Figure 3. Description of the two-steps procedure used for the simulation. We scan all the points for a given region $\Re$ between the two wells. The density of points depends on the wavelength of the wave used to scan the formations. At each scanning point, we place a seismic source (e.g. a Ricker wavelet) and record the seismograms at the positions of all the seismic sensors located in the wells. We then re-inject the recorded seismograms in the formation in order to focus at the position of the scanning point (time reversal). The voltage is simulated at the focusing time at a set of electrodes Pi (the reference of the voltage is at infinity). This voltage is reported at the focus position; a map of these voltages obtained for a collection of scanning points generates a 'seismoelectric image' usable as a physical constraint for electrical tomography (Step 2).

Downloaded from http://gji.oxfordjournals.org/ at Colorado School of Mines on June 26, 2014

3 STEP 1: THE SEISMOELECTRIC FOCUSING

We illustrate our method using a heterogeneous material that is bimodal in terms of the distribution of its material properties (Fig. 2). For instance one phase represents the porous material saturated with water and the other the porous material partially saturated with oil. The properties of these 'reservoir' and 'non-reservoir' rocks are provided in Table 1. Fig. 2(c) shows the position of two wells in which seismic receivers are placed. The goal is to scan all the space indicated by the yellow rectangle in Fig. 2(c) (scanning domain $\Re$). The entire procedure is summarized in the chart shown in Fig. 3.

There are two main ways in which we can implement our procedure in practice:

(1) First, we could consider a broad distribution of sources located at all locations in the boreholes. These sources are characterized by different phase delays, but are synchronized such that the generated acoustic energy focuses at a specified location in the subsurface. Every focus location requires a different physical experiment with sources characterized by different phase delays. The effort required by this experimental setup is proportional with the number of scanning points in the subsurface.

(2) Second, we could consider a single source located at different points in the boreholes. We simulate waves separately from every point in the borehole and recombine linearly the resulting wavefields and electrical potential fields to reflect delays that would focus energy at a given point in the subsurface. In this case, the effort is proportional to the number of sources in the boreholes, since we can consider the computational effort to recombine the electrical potential fields negligible.

In the numerical experiment shown below, we use an even simpler method. We loop over all the points located in the scanning area and inject an identical pulse (Ricker wavelet) to generate wavefields propagating in the medium. We assume that we know the velocity model with sufficient accuracy in order to predict correctly the kinematics in the subsurface. Fig. 4 shows an example of wave propagation from a scanning point to the receivers located in the wells. The seismic wavefield encodes the model heterogeneities and carries this information to the boreholes surrounding the scanning point. Then, we simulate the acquisition of these seismic signals at the receivers located in the wells (see the seismograms in Fig. 5) and we re-inject the recorded seismograms into the modelled formation in order to focus the seismic energy back at the chosen scanning point (Fig. 6). As indicated earlier, the recorded seismograms (see Fig. 5) could be generated by linear superposition of seismograms generated separately from all points in the boreholes.

The backpropagating waves (Fig. 6) generate seismoelectric sources at every location where rapid changes of physical properties occur in the medium (Fig. 7). The corresponding normalized electric potential distribution is shown in Fig. 8. The reason for normalization of the potential map is that the source we use is of arbitrary strength, and this in turn means that the virtual electrode obtained by focusing is characterized by a proportional potential. However, since the potential normalization is done globally, that

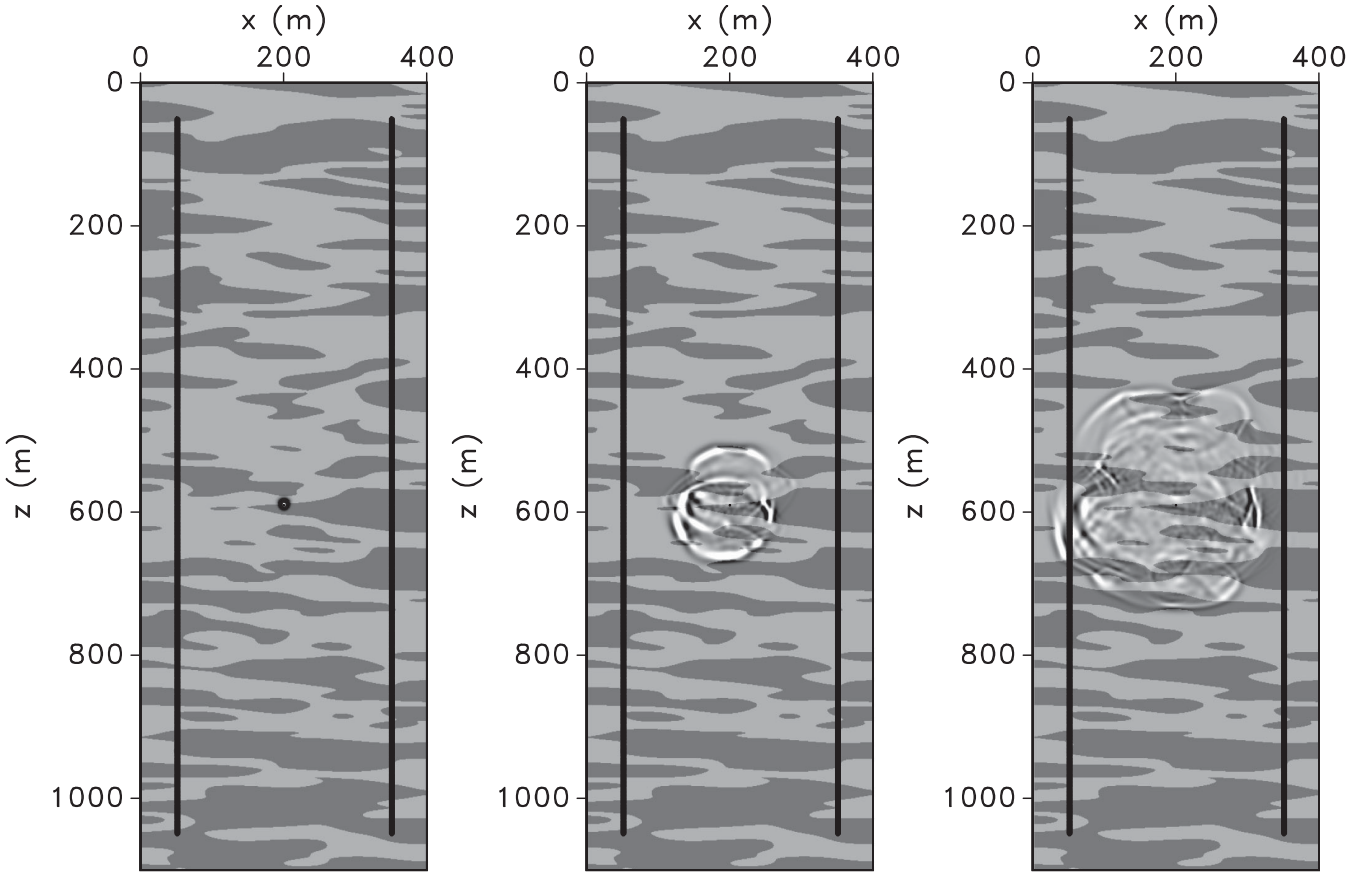


Figure 4. Seismic wavefields from a seismic source located at one of the scanning locations belonging to the scanning domain $\Re$. The seismic wavefield spreads throughout the medium and reaches the seismic receivers located in the two wells. The corresponding seismograms are recorded at these seismic receivers (see Fig. 5).

Downloaded from http://gji.oxfordjournals.org/ at Colorado School of Mines on June 26, 2014

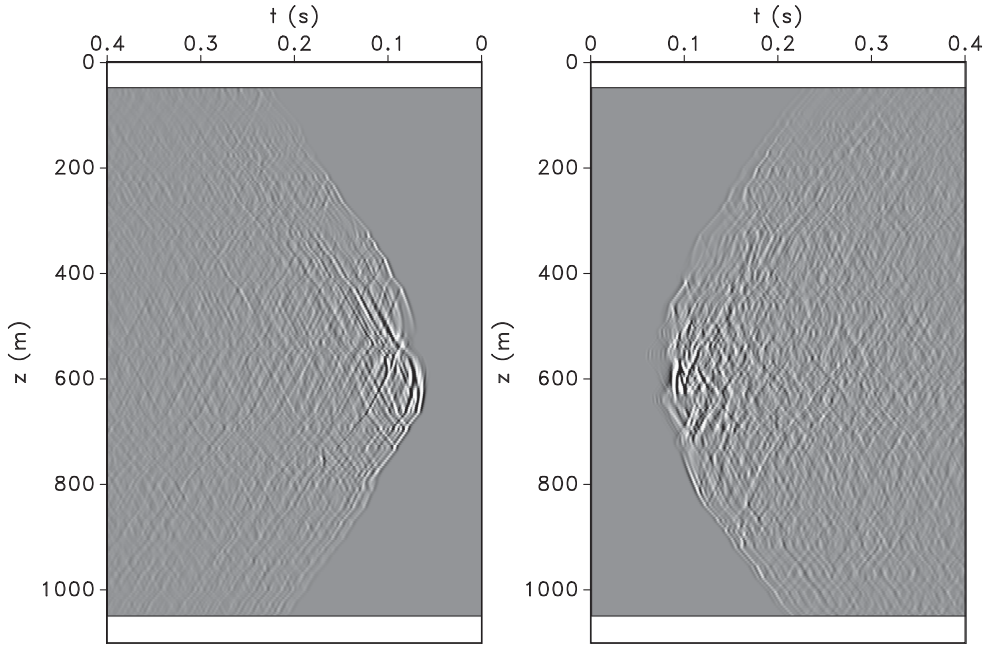


Figure 5. The propagating wavefield recorded at the seismic receivers in the two boreholes located in the vicinity of the scanning area. Similar seismograms could be obtained by linear superposition of seismograms generated from individual locations in the boreholes, after appropriate phase delay corresponding to the desired focusing point in the region $\Re$.

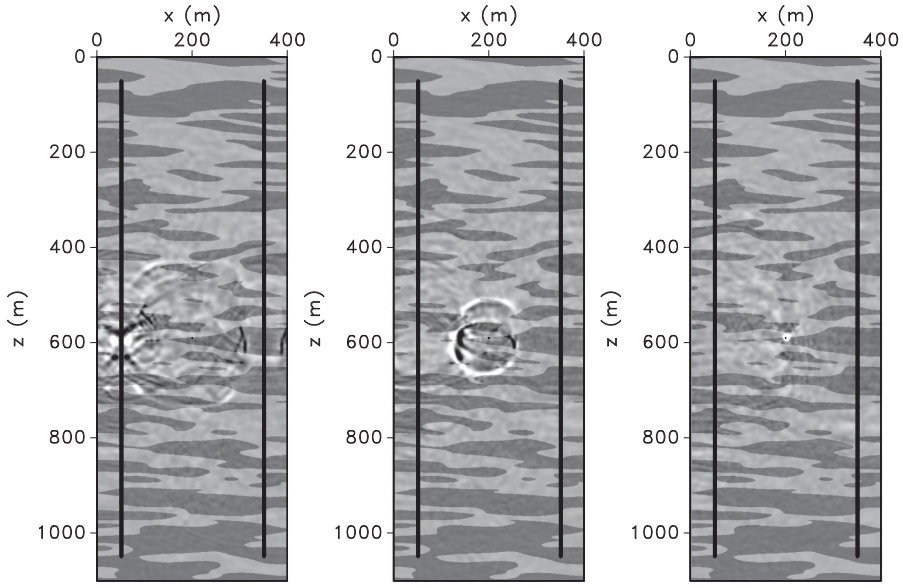


Figure 6. Seismic wavefield obtained by backpropagating the recorded seismic signals into the medium in order to focus seismic energy at the location of the original scanning point (time reversal). In this case, the seismograms do not need to be delayed since they are generated through modelling from the desired focusing point.

is for all time steps, the relative relationships between the potential reconstructed at different times and positions is preserved. The simulation shown in Figs 4–8 illustrates the main difficulty of seismoelectric investigation of the subsurface: relatively weak sources of energy are located everywhere in the medium, and at all times. Our method, however, addresses these challenges. Instead of observing the seismoelectric conversions at all times, we concentrate on only one moment, t the time when the injected wavefield focuses on the desired scanning point. In this case, we know precisely the source of electric current position and time, and we also maximize the strength of the source. The number of focus points is determined from the wavelength of the wave; we typically use 2 focus points per wavelength.

We repeat the process outlined earlier, and record the electric potential at a small number of electrodes located in the two wells. These electrodes record the electrical potential over time, but we only use the voltage observed at the focusing time. This is mainly because the seismoelectric sources prior to the focus time are distributed everywhere in the medium. This distribution does not allow us to associate an observed electric potential with a given position

Downloaded from http://gji.oxfordjournals.org/ at Colorado School of Mines on June 26, 2014

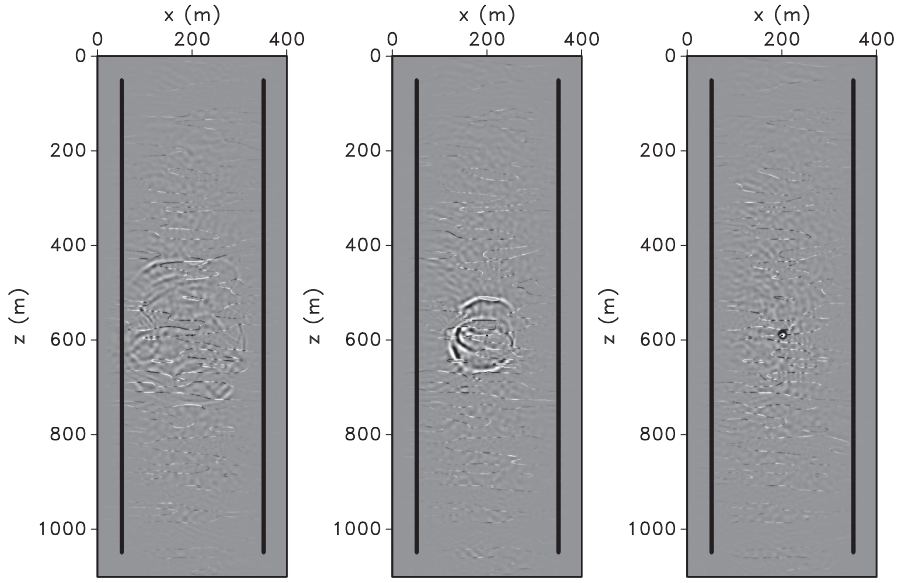


Figure 7. The backpropagating wavefields (for the three snapshots shown in Fig. 6) generate seismoelectric current sources at many locations characterized by appropriate contrasts of physical properties. The seismoelectric source is thus distributed in space and time, which creates strong interpretation ambiguity. However, at the focusing time, the seismoelectric current source is mostly localized in space and it is stronger than at other times. We don't plot the scale of the seismoelectric current source here because they depend on the intensity of the seismic source.

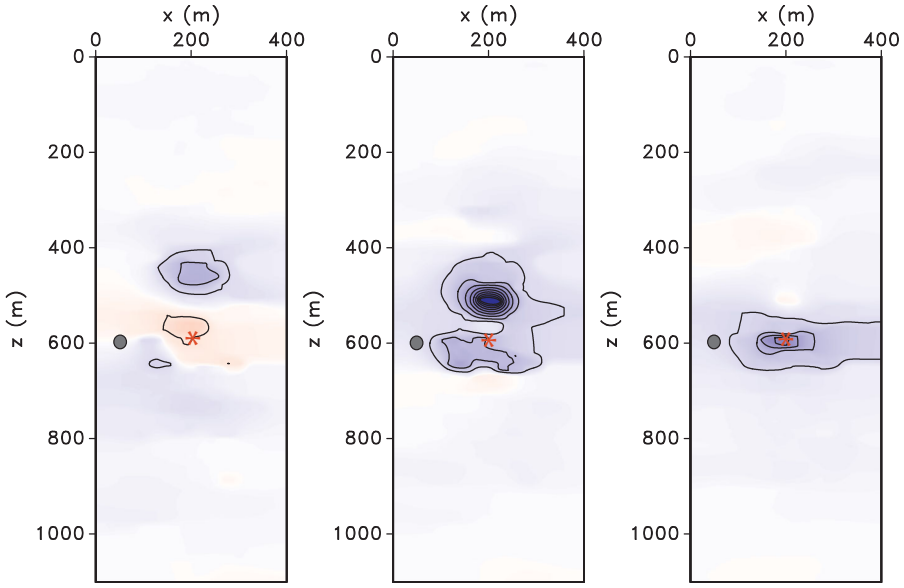


Figure 8. Electrical potential observed as a function of time for the seismoelectric sources depicted in Fig. 7 and corresponding to the three snapshots shown in Fig. 6. The filled circle corresponds to the position of the simulated recording electrode while the red star corresponds to the focusing point. Interpretation of this potential is ambiguous, given that the seismoelectrical source is distributed in space and time. In our method, only the potential seen in the rightmost frame is relevant and its interpretation is not ambiguous since in this case we deal with a known position and time of the source. We do not plot the scale of the electrical potential because they depend on the intensity of the seismic source, which is arbitrary. The only thing that matters is that the strength of the electrical potential is recordable at the electrodes located in the two wells.

in the subsurface, thus causing interpretation ambiguity, which can be resolved by restricting our attention just to the time when the seismic focusing occurs. Fig. 9 shows seismoelectric potential maps observed at a set of given electrodes in the wells. For each electrode, the seismoelectric potential map is obtained by focusing the seismic energy at each of the 40 960 locations in the target area $\Re$. Although the potential would be measured in a real experiment at a set of electrodes in the well, we report all the simulated measurements at their corresponding focus positions, thus generating these seismoelectric maps of the subsurface highlighting the locations characterized by hydroelectrical contrasts. We note that these maps are also subject to 'illumination' from a given electrode—the potential weakens with distance and as a function of the distribution of conductivity in the medium, so different electrodes are sensitive to different portions of the subsurface. Such maps are shown for various electrodes in Fig. 9. A cumulative map of the absolute value of the electrical potential is

Downloaded from http://gji.oxfordjournals.org/ at Colorado School of Mines on June 26, 2014

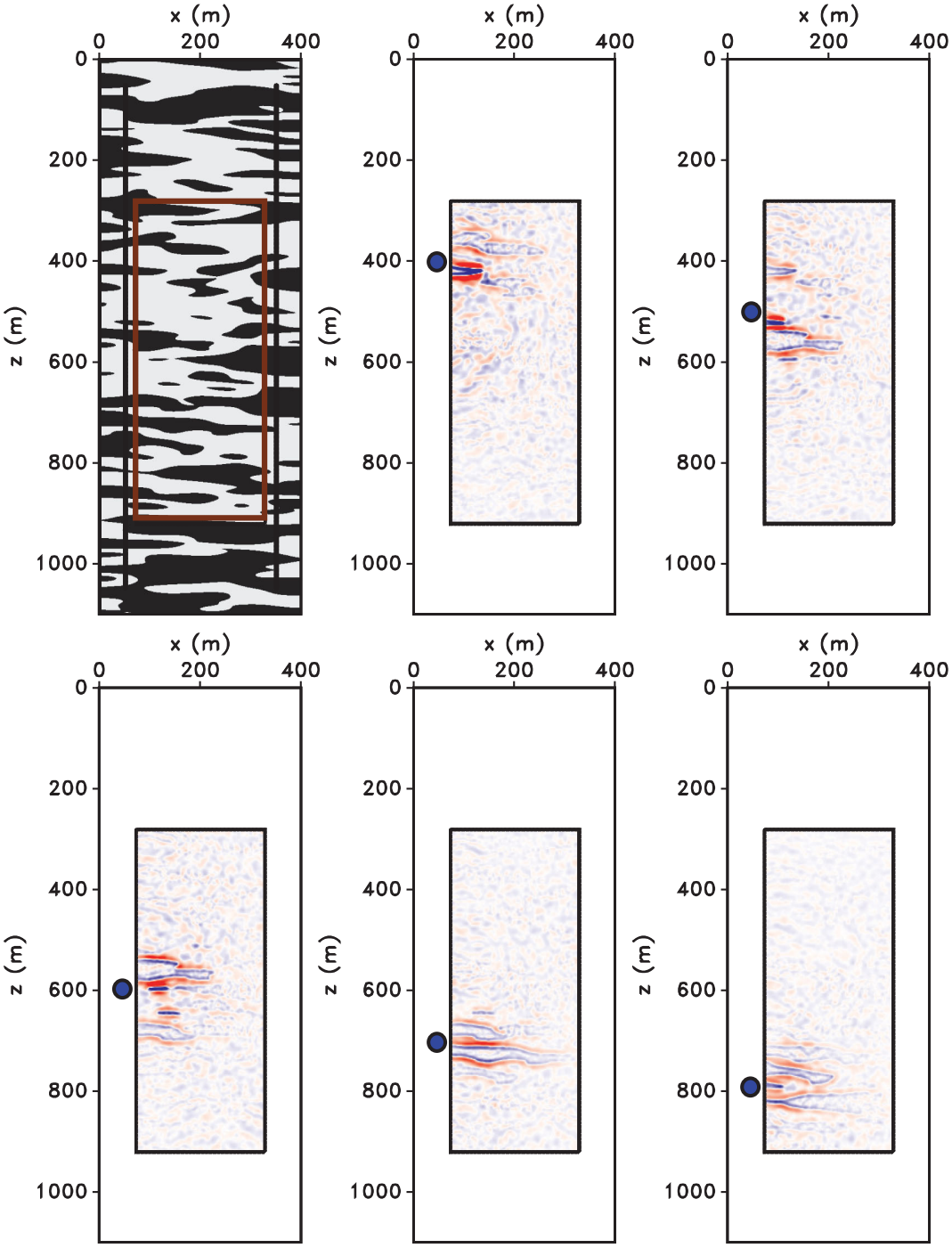


Figure 9. Seismoelectric potential maps numerically observed at a set of given electrodes in the wells) the large filled circles). For each electrode, the seismoelectric potential map is obtained by focusing the seismic energy at each of the 40 960 locations in the target area $\Re$. Although the potential would be measured in a real experiment at a set of electrodes in the well, we report all the simulated measurements at their corresponding focus positions. The electrical potential map illuminates the heterogeneities in the vicinity of the electrode (the reference electrode is supposed to be at infinity). Far from the simulated electrodes, the electrical potential is too weak (in a relative sense) to image the heterogeneities.

shown in Fig. 10. This 'seismoelectric image' illuminates the position of all heterogeneities in the scanning area located between the boreholes.

In the next section, we use the structural information contains in this seismoelectric image to guide the inversion of electrical resistivity data with current sources and potential receivers located in the two wells.

4 STEP 2: APPLICATION OF IMAGE-GUIDED INVERSION TO ERT

In this section, we consider a set of electrodes located in the two wells with a spacing of $L = 10$ meter between the electrodes. Using the map of electric potential defined in the previous section, we can proceed to the next step, that is invert for the distribution of

Downloaded from http://gji.oxfordjournals.org/ at Colorado School of Mines on June 26, 2014

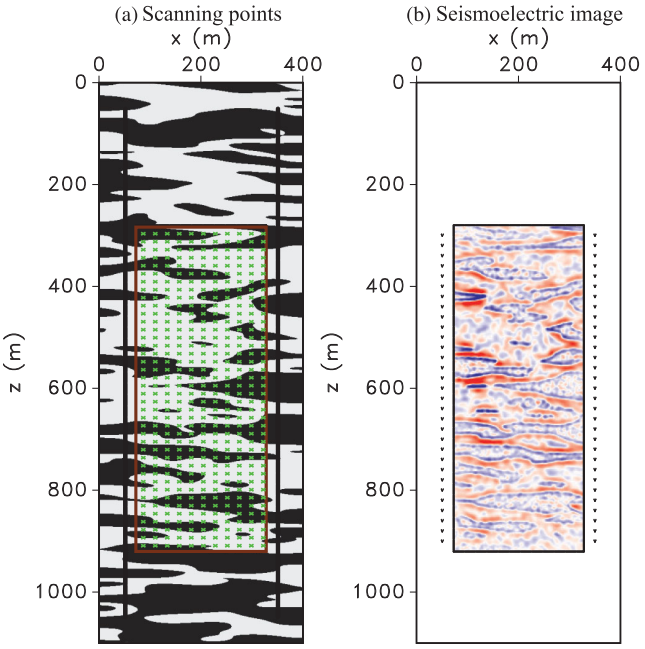


Figure 10. Seismoelectric image of the electrical potential using a set of electrodes located in the two wells for the domain $\Re$. (a) Position of all the scanning (focusing) points. The number of scanning points is $(Nx = 128) \times (Nz = 320)$, that is a total of more than 40 960 points. Only a fraction of these points is shown here (b) High definition voltage map with the position of the electrodes used in the wells to scan the electrical potential. We see that the voltage map contains a lot of structural information regarding the position of the heterogeneities between the wells in the scanning area. The voltages are opposite in sign on each side of the heterogeneities.

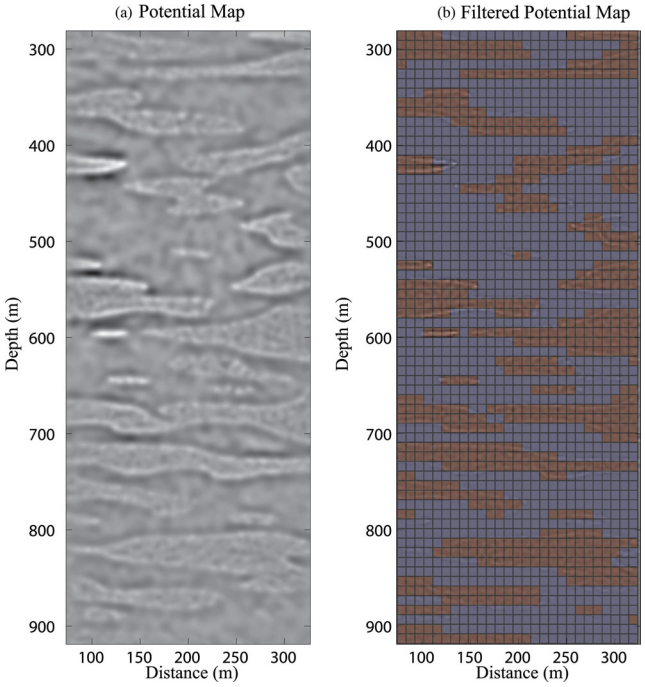


Figure 11. Structural map. (a) Edge detection from the potential map using an image sharpening filter in domain $\Re$. This is done with the image processing toolbox of Matlab (function imsharpen, see http://searchcode.com/codesearch/view/13889955). (b) The discretized structural information map determined from the filtered seismoelectric potential map is used to impose textural information to the electrical resistivity tomogram.

electrical conductivity in the medium using apparent resistivity data acquired with a set of electrodes located in the two wells. We show in this section that this method may improve substantially cross-well electrical resistivity tomography (ERT).

4.1 Edge detection

First, we filter the seismoelectric image to detect the boundaries of the different formations. Among numerous techniques available to detect the edge, in this work we used a simple approach of image sharpening (Fig. 11). Once the boundaries are identified, we discretize the domain between the two wells in $L \times L$ m cells (based on the electrodes separation of L) to get the structural discretized image shown in Fig. 11(b). All cells that fall within the boundaries are considered to belong to the same unit.

4.2 Introduction of structural information into the objective function

We consider again our two vertical wells A and B, located 300 m apart and with depth of 1050 m. Within each borehole, we consider 105 electrodes per borehole (see Fig. 12a). We simulate bipole–bipole data (one injection source and one measurement electrode in each borehole) with a total of 19 292 measurements.

The next step is to invert these apparent resistivity data. In electrical impedance (resistivity) tomography, we traditionally use a least-square minimization of the following objective function $P^{\beta}(\boldsymbol{X})$ with the L2-norm to find an optimal resistivity model $\boldsymbol{X}^*$ (e.g. Oware *et al.* 2012)

$$\boldsymbol{X}^* = \arg\min P^{\beta}(\boldsymbol{X}), \tag{14}$$

$$P^{\beta}(\boldsymbol{X}) = [\boldsymbol{d} - G(\boldsymbol{X})]^T \boldsymbol{C}_d^{-1} [\boldsymbol{d} - G(\boldsymbol{X})] + \beta [\boldsymbol{X} - \boldsymbol{X}_0]^T C_m^{-1} [\boldsymbol{X} - \boldsymbol{X}_0], \tag{15}$$

where $P^{\beta}(\boldsymbol{X})$ is the sum of a data misfit function (first term) and a model objective function (second term), which is used for the regularization of the inverse problem. In this equation, $\boldsymbol{X}$ denotes the 2.5-D resistivity model (vector of model parameters, note that we estimate the log-conductivity distribution to enforce positivity of the resistivity of each cell), $\boldsymbol{X}_0$ a prior resistivity model (we will not use such a model hereinafter), $\boldsymbol{G}$ denotes the non-linear forward operator to map the predicted data given a resistivity model $\boldsymbol{X}$, $\boldsymbol{d}$ denotes the vector of measured apparent resistivity (measured data vector), $\boldsymbol{C}_d^{-1}$ denotes the inverse data covariance matrix (taken diagonal and based on the variance on the measurements), β is the regularization parameter balancing the data misfit function and the model objective function and $\boldsymbol{C}_m^{-1}$ is the inverse model covariance matrix.

In the classical least-square inversion, $\boldsymbol{C}_m^{-1}$ is a square $n \times n$ matrix (n denotes the number of model cells) corresponding to model-weighting regularization matrix (the discretized Laplacian operator of the model). The resistivity model is updated using an

Downloaded from http://gji.oxfordjournals.org/ at Colorado School of Mines on June 26, 2014

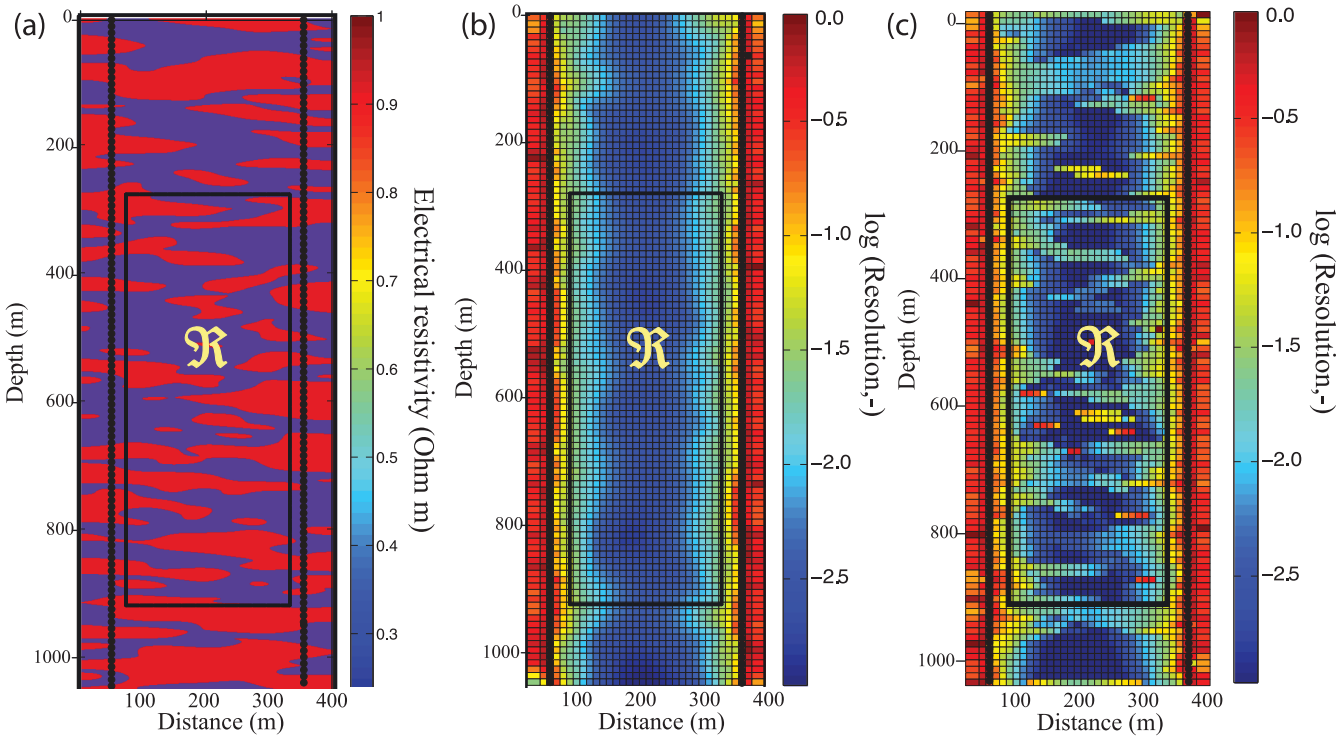


Figure 12. Geometry and sensitivity of the electrode array. (a) Position of the electrodes (black circles, 105 electrodes per well, spacing 10 m) for the cross-well resistivity tomography and discretization of the domain (the size of the cells is 10 m × 10 m). The resistivity image denotes the true resistivity image used to perform to simulate the acquisition of the apparent resistivity data. We are interested in recovering the resistivity information in domain $\Re$. (b) Sensitivity map (the diagonal of the resolution matrix) of the electrode array used for the tomography. We see that good sensitivity in conventional electrical resistivity tomography based on isotropy smoothing is limited to the vicinity of the electrodes. (c) Sensitivity map using the structural information from the seismoelectric coupling (computation done at the last iteration using the light constraint, $\beta = 0.1$.

iterative approach based on the equations

$$\left[\boldsymbol{J}^T \boldsymbol{C}_d^{-1} J + \beta \left(\boldsymbol{C}_m^{-1}\right)^T \boldsymbol{C}_m^{-1}\right] \Delta \boldsymbol{X} = \boldsymbol{J}^T \boldsymbol{C}_d^{-1} \left[\boldsymbol{d} - G(\boldsymbol{X}_{k-1})\right] - \beta \left(\boldsymbol{C}_m^{-1}\right)^T \boldsymbol{C}_m^{-1} \boldsymbol{X}_{k-1}, \quad (16)$$

$$\boldsymbol{X}_k = \boldsymbol{X}_{k-1} + \Delta \boldsymbol{X}, \quad (17)$$

where $\boldsymbol{X}_k$ and $\boldsymbol{X}_{k-1}$ are the models at iteration k and (k–1), respectively (the initial model is constant), $\Delta \boldsymbol{X}$ denotes the model update at iteration k and **J** denotes the Jacoban matrix with elements $J_{ij} = \partial d_i / \partial X_j$ with d_i being the calculated value of measurement i. The Jacobian matrix is updated at each iteration. The inversion continues until either a target rms error is reached, or a prescribed number of iteration is reached, or the difference in the rms error between two iterations is smaller than a prescribed value. In our example below, we used the condition among the three conditions that comes first: (1) The maximum number of iteration (fixed to 8) is reached; (2) if the rms increases, the inversion is stopped and (3) if two sequential iterations correspond to less than 2 per cent in relative value, we stop the inversion.

The model resolution matrix relating the inverted with the true model

$$\boldsymbol{X} = \boldsymbol{R} X_{true}, \quad (18)$$

is defined by (Menke 1984),

$$\boldsymbol{R} = \left[\boldsymbol{J}^T \boldsymbol{C}_d^{-1} \boldsymbol{J} + \beta \left(\boldsymbol{C}_m^{-1}\right)^T \boldsymbol{C}_m^{-1}\right]^{-1} \boldsymbol{J}^T \boldsymbol{C}_d^{-1} \boldsymbol{J}, \quad (19)$$

based on the Jacobian **J** and on the regularization parameter β from the final iteration. For each cell of the discretized resistivity model, the sensitivity of the data to determine the value of the resistivity of this cell is determined from the diagonal elements of the model resolution matrix. Therefore, incorporating structural information into the matrix $\boldsymbol{C}_m^{-1}$ leads to better resolution. From Figs 12(b) and (c), we can compare the resolution of the resistivity tomogram without and with structural constraints. With isotropic smoothing, the resolution is good only in the vicinity of the electrodes. However, when we introduce structural information in the model covariance, we improve the resolution of the method and better constrain the structural features located in the central part of the domain between the two wells.

The classical inversion of the apparent resistivity data with no structural information (isotropic smoothing) is shown in Fig. 13. As expected, this approach yields a very smooth resistivity image because of the lack of resolution far from the electrodes. In addition, the true values of the electrical resistivity are not well recovered.

The question is what would be the effect of incorporating the structural information contained in the seismoelectric image into the resistivity inversion. In this work, since we are able to identify the boundaries with the SeismoElectric Focusing approach, we assign equal weights to neighbouring cells only if they belong to the same unit (Fig. 14). This way, we incorporate directly structural information into the objection function, by changing only the matrix $\boldsymbol{C}_m^{-1}$. A detailed approach on how this structural information is incorporated in $\boldsymbol{C}_m^{-1}$ can be found in a number of papers (e.g. Farquharson 2008; Hale 2009a,b,c; Lelièvre & Farquharson 2013; Zhou *et al.* 2014).

Downloaded from http://gji.oxfordjournals.org/ at Colorado School of Mines on June 26, 2014

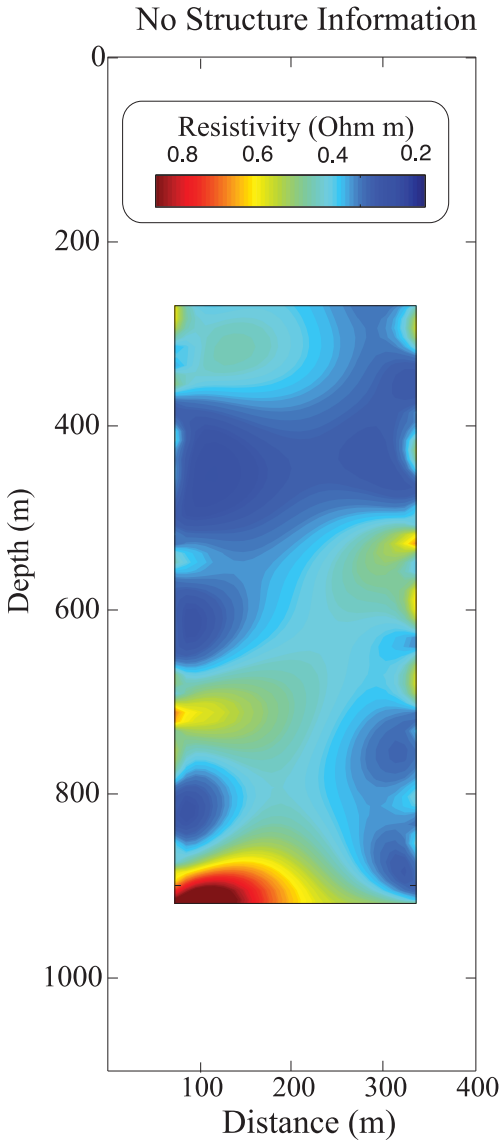


Figure 13. Result of a classical cross-well resistivity tomography in domain $\Re$ using the least-square method with no structural information used to constrain the model covariance matrix (isotropic smoothing). We use the bipole–bipole array (one injection source and one measurement electrode in each borehole) with a total of 19 292 measurements. Classical cross-well resistivity tomography is unable to image the formations between the wells due to a lack of resolution far away from the electrodes. In addition, the values of the resistivity are smoother than the true values, which mean that the application of a petrophysical model to the recovered resistivity would lead to a misinterpretation of the petrophysical parameters of interest.

4.3 Results

In the following, we study of the effect of the structural information on the recovered model. The L-curve method can be used in principle to find the optimal value of the regularization parameters. However, since in our method we enforce structural information, finding an appropriate regularization parameter with the L-curve is not necessarily the optimal way to proceed. For our tests, we considered the following values of the regularization parameter β: 0.1 (light), 1 (medium), 10 (hard) and 100 (extreme; see Fig. 15). A typical value for the L2 scheme is on the range of 0.01–0.1 using the L-curve approach. For our image-guided scheme, we enforce a constant value for all the five iterations. Larger values of the Lagrange parameter β enforce the structural similarity within each layer (conductivity values show less variation within each formation) and have a negative effect on the data rms. We see clearly from Fig. 15 that the texture of the resistivity tomogram is improved and that the resistivity values are closer to the true resistivity value by comparison with the tomogram obtained in Fig. 13. Such an improvement is very important to be able to apply reliably petrophysical model to transform resistivity or complex conductivity in terms of relevant parameters such a saturation, salinity, porosity, or permeability.

Finally in Fig. 16, we show the convergence curves for the inversion. Both the Gauss–Newton inversion with and without structural constraints converge in few iterations. The inversion without structural constraints (isotropic smoothing) converges to a slightly lower rms data misfit than the image-guided inversion. That said, this is expected since in the image guided inversion, the inversion is a trade-off between respecting the guiding image and honouring the data at the same time.

5 DISCUSSION

Three main points deserve to be discussed in greater detail: (1) How the seismoelectric focusing could be done in practice? (2) How do we derive the velocity model required for focusing? (3) What is the signal-to-noise ratio for the seismoelectric conversions?

The first point, briefly discussed above, is related to the focusing methodology which has significant practical implications. As indicated earlier, we can consider two main approaches. In the first approach, we can use many sources at elastic energy activated at different locations in space at the same time. Waveforms injected into the medium with appropriate delays depending on the source position concentrate at the desired focus point and potentially trigger strong seismoelectric conversions. The drawbacks of this approach is that multiple elastic sources need to be available in the field at a given time, which is costly, and that the sources need to be precisely synchronized, which is technically difficult. A second approach is to use a single source of elastic energy in the field, but activate it multiple times at different positions in space. Then, we can recombine the observed electric responses numerically based on timing that would be needed for the elastic energy to focus at a given location in the medium. The drawbacks of this approach is that the duration of the experiment is longer, since the elastic source is activated multiple times at different locations, and that the observed electric field for each individual source might be hampered by coherent or incoherent noise in the field. In both situations, it is desirable to have access to the time function of the source, for example use a borehole or surface vibrator.

The second point to discuss is the necessity of an accurate velocity model. Precise focusing in the subsurface requires a good understanding of the velocity model. This implies that prior to the seismoelectric analysis, we construct the velocity model using best-in-class tools, like waveform inversion (e.g. de Barros *et al.* 2010). This is a feasible setup, since our method is designed for monitoring the subsurface, for example of a producing reservoir, in which case we have the opportunity to precede the seismoelectric procedure with conventional seismic tomography.

Finally, we conclude by discussing the signal-to-noise ratio of the seismoelectric conversions. We have shown that by focusing seismic waves at a set of points, we can image the structural heterogeneities of the formations. We have not discussed the order of magnitude of the electrical field produced by the seismoelectric coupling for three

Downloaded from http://gji.oxfordjournals.org/ at Colorado School of Mines on June 26, 2014

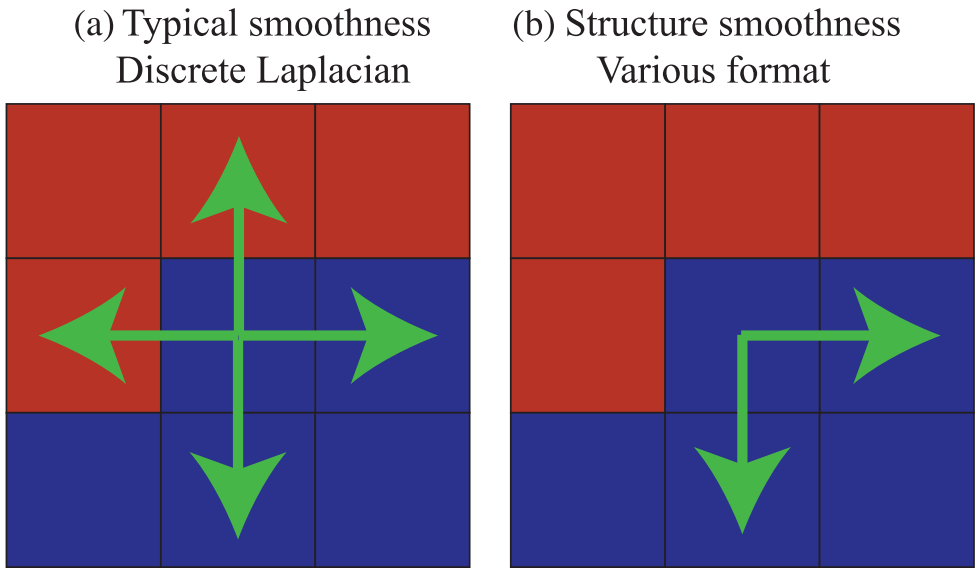


Figure 14. Computation of the smoothing matrix using the detection of boundaries. (a) The classical discrete Laplacian correlates each pixel with its neighbours in an isotropic way (isotropic smoothing). (b) The structural constrains correlate only neighbour pixel that belong to the same unit. In our approach, the structural constraints are imposed from the seismoelectric image and used to define locally a smoothing matrix that spreads information along the interfaces, but not across them. The image used to provide the structural information is the one shown in Fig. 11(b).

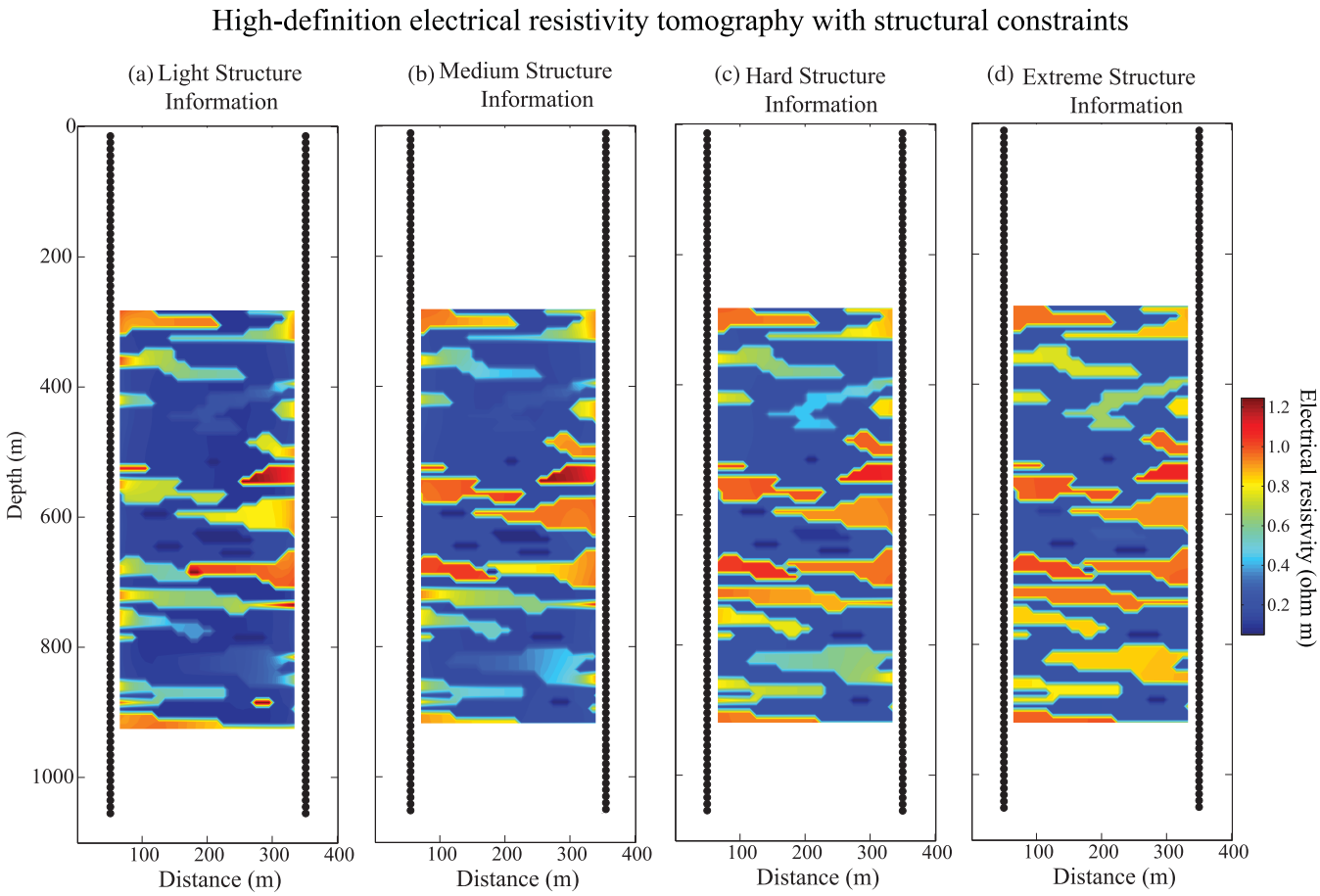


Figure 15. Importance of structural information in recovering the cross-well resistivity model through cross-well resistivity tomography. We considered the following values of the regularization parameter β: 0.1 (light), 1 (medium), 10 (hard) and 100 (extreme). Compared to Fig. 13, we observe a strong improvement in the resolution of the electrical resistivity tomogram.

Downloaded from http://gji.oxfordjournals.org/ at Colorado School of Mines on June 26, 2014

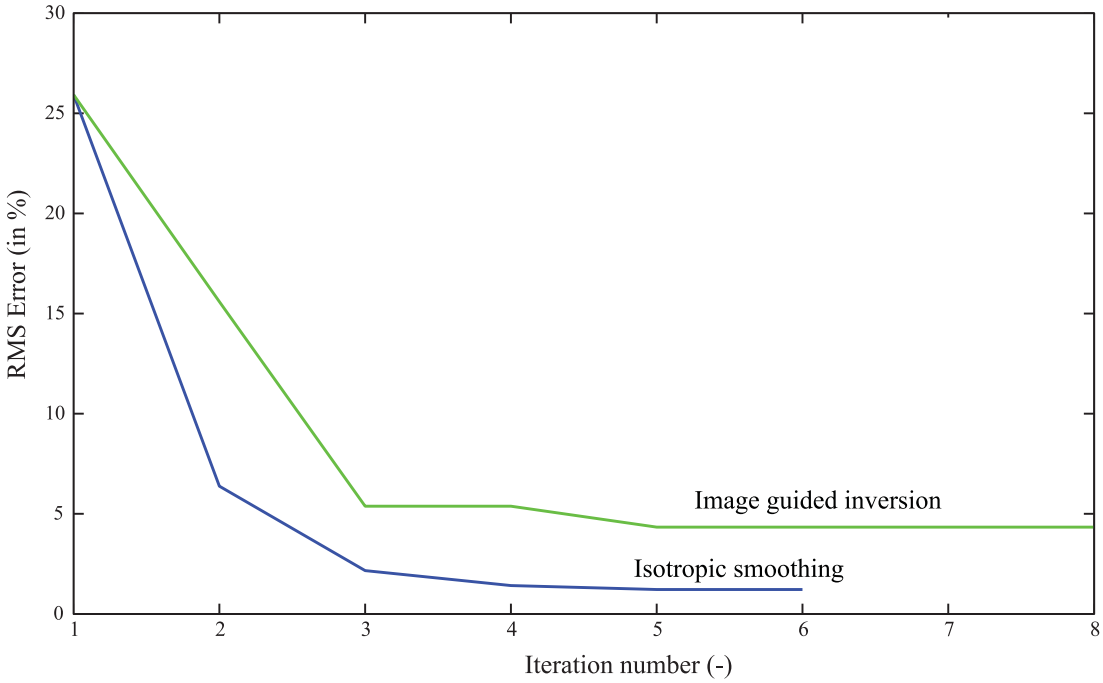


Figure 16. Decrease of the data misfit root mean square error versus the number of iteration in the Gauss–Newton inversion. We see that the inversion with isotropic smoothing converges to a slightly smaller rms error by comparison with the inversion with structural constraints.

fundamental reasons: (1) We are not directly interested in the amplitude of the electrical potentials when we built the seimoelectric image. Indeed, the only thing that matters in building the seismoelectric image displayed in Fig. 10 are the local relative variations of the electrical potentials that map heterogeneities. (2) The seismoelectric conversions need only to be higher than the background noise. In wells, the electrical noise is on the order of 0.1 μV m^{-1} for the electrical field (but it can decrease down to 1 nV m^{-1} at depth or at the sea floor) and the signals can be on the order of few μV m^{-1} (Dupuis *et al.* 2009). In land seismoelectric studies, the noise level can be on the order of 0.1 μV m^{-1} s well (see for instance fig. 3 of Dupuis *et al.* 2007), (3) If the signal-to-noise ratio is not good, stacking may be required. One way to stack seismoelectric signals would be to repeat the same seismic experiment from the same source positions. Another possibility would be to inject a harmonic pressure source and to stack the resulting harmonic electrical field over the number of cycles needed to have an acceptable signal-to-noise ratio. Therefore in principle, there should be no issues in building the seimoelectric image required to perform the image-guided inversion of ERT data.

6 CONCLUSIONS

We have developed a new and simple geophysical method that could be used to map heterogeneities in resistivity between a set of wells. This method is based on scanning, through seismic focusing and electrokinetic conversion, of the electrical potential between two wells. The focusing is done through time reversal of the seismic waves using a set of seismic sources located in two wells. The obtained 'seismoelectric image' contains structural information regarding the heterogeneities. In a second step, this image is used to constrain resistivity tomography using image-guided inversion imposing structural constraints in the model covariance matrix. This approach opens new perspective in imaging the fine resistivity structure between wells and then interpreting the resistivity structure in terms of petrophysical properties of interest. This method could be applied to complex conductivity, which is known to contain information that can be used to determine the permeability field between wells.

ACKNOWLEDGEMENTS

We thank Colorado School of Mines for funding this research though a grant to AR and PS. We thank Dave Hale for fruitful discussions regarding image-guided inversion.

REFERENCES

Bolève, A., Crespy, A., Revil, A., Janod, F. & Mattiuzzo, J.L., 2007. Streaming potentials of granular media: influence of the Dukhin and Reynolds numbers, *J. geophys. Res.,* **112,** B08204, doi:10.1029/2006JB004673.

Butler, K.E., 1996. Measurement of the seismoelectric response from a shallow boundary, *Geophysics,* **61**(6), 1769–1778.

Chapman, D.L., 1913. A contribution to the theory of electrocapillarity, *Phil. Mag.,* **25**(6), 475–481.

Davis, J.A., James, R.O. & Leckie, J., 1978. Surface ionization and complexation at the Oxide/water interface, *J. Colloid Interface Sci.,* **63,** 480–499.

De Barros, L., Dietrich, M. & Valette, B., 2010, Full waveform inversion of seismic waves reflected in a stratified porous medium, *Geophys. J. Int.,* **182**(3), 1543–1556.

Dupuis, J.C. & Butler, K.E., 2006. Vertical seismoelectric profiling in a borehole penetrating glaciofluvial sediments, *Geophys. Res. Lett.,* **33,** L16301, doi:10.1029/2006GL026385.

Dupuis, J.C., Butler, K.E. & Kepic, A.W., 2007. Seismoelectric imaging of the vadose zone of a sand aquifer, *Geophysics,* **72**(6), A81–A85.

Dupuis, J.C., Butler, K.E., Kepic, A.W. & Harris, B.D., 2009. Anatomy of a seismoelectric conversion: measurements and conceptual modeling in boreholes penetrating a sandy aquifer, *J. geophys. Res.,* **114,** B10306, doi:10.1029/2008JB005939.

Downloaded from http://gji.oxfordjournals.org/ at Colorado School of Mines on June 26, 2014

Farquharson, C.G., 2008. Constructing piecewise-constant models in multi-dimensional minimum-structure inversions, *Geophysics,* **73,** K1–K9.
Frenkel, J., 1944. On the theory of seismic and electroseismic phenomena in a moist soil, *J. Phys.,* **8**(4), 230–241.
Garambois, S. & Dietrich, M., 2001. Seismoelectric wave conversions in porous media: field measurements and transfer function analysis, *Geophysics,* **66**(5), 1417–1430.
Gouy, G.L., 1910. Sur la constitution de la charge électrique à la surface d'un électrolyte, *Journal de Physique Théorique et Appliquée,* **9**(4), 457–468.
Günther, T., Rücker, C. & Spitzer, K., 2006. Three-dimensional modeling and inversion of dc resistivity data incorporating topography—II. Inversion, *Geophys. J. Int.,* **166,** 506–517.
Haas, A.K., Revil, A., Karaoulis, M., Frash, L., Hampton, J., Gutierrez, M. & Mooney, M., 2013. Electrical potential source localization reveals a borehole leak during hydraulic fracturing, *Geophysics,* **78**(2), D93–D113.
Hale, D., 2009a. Structure-oriented smoothing and semblance, *CWP Rep.* **635,** Available at: http://inside.mines.edu/~dhale/papers/Hale09StructureOrientedSmoothingAndSemblance.pdf (last accessed 22 January 2014).
Hale, D., 2009b. Image-guided blended neighbor interpolation, *CWP Rep.,* **634,** Available at: http://inside.mines.edu/~dhale/papers/Hale09ImageGuidedBlendedNeighborInterpolation.pdf (last accessed 22 January 2014).
Hale, D., 2009c. Image-guided blended neighbor interpolation of scattered data, in *Proceedings of the 79th Annual International. Meeting, SEG, Expanded Abstracts*, **28,** pp. 1127–1131.
Jardani, A., Revil, A., Bolève, A., Crespy, A., Dupont, J.-P., Barrash, W. & Malama, B., 2007. Tomography of the Darcy velocity from self-potential measurements, *Geophys. Res. Lett.,* **34,** L24403, doi:10.1029/2007GL031907.
Jardani, A. *et al.*, 2009. Reconstruction of the water table from self-potential data: a Bayesian approach, *Ground Water,* **47**(2), 213–227.
Jardani, A., Revil, A., Slob, E. & Söllner, W., 2010. Stochastic joint inversion of 2D seismic and seismoelectric signals in linear poroelastic materials: a numerical investigation, *Geophysics,* **75**(1), N19–N31.
Jougnot, D., Rubino, J.G., Rosas Carbajal, M., Linde, N. & Holliger, K., 2013. Seismoelectric effects due to mesoscopic heterogeneities, *Geophys. Res. Lett.,* **40,** doi:10.1002/grl.50472.
Kemna, A. 2000. *Tomographic inversion of complex resistivity, Dissertation*, Ruhr Universität Bochum, Germany.
Kulessa, B., Murray, T. & Rippin, D., 2006. Active seismoelectric exploration of glaciers, *Geophys. Res. Lett.,* **33,** L07503, doi:10.1029/2006GL025758.
Lelièvre, P.G. & Farquharson, C.G., 2013. Gradient and smoothness regularization operators for geophysical inversion on unstructured meshes, *Geophys. J. Int.,* **178,** 623–637.
Leroy, P. & Revil, A., 2004. A triple layer model of the surface electrochemical properties of clay minerals, *J. Colloid Interface Sci.,* **270,** 371–380.
Leroy, P. & Revil, A., 2009. Spectral induced polarization of clays and clay-rocks, *J. geophys. Res.,* **114,** B10202, doi:10.1029/2008JB006114.
Leroy, P., Revil, A., Kemna, A., Cosenza, P. & Gorbani, A., 2008. Spectral induced polarization of water-saturated packs of glass beads, *J. Colloid Interface Sci.,* **321,** 103–117.
Loke, M. & Barker, R., 1995. Least-squares deconvolution of apparent resistivity pseudosections, *Geophysics,* **60**(6), 1682–1690.
Loke, M.H. & Lane, J.W., 2002. The use of constraints in 2D and 3D resistivity modeling, in *Proceedings of the 8th meeting of the Environmental and Engineering Geophysical Society, – European section,* Averio, Portugal, p. 4.
Mahardika, H., Revil, A. & Jardani, A., 2012. Waveform joint inversion of seismograms and electrograms for moment tensor characterization of fracking events, *Geophysics,* **77**(5), ID23–ID39.
Menke, W., 1984. The resolving power of cross-borehole tomography, *Geophys. Res. Lett.,* **11**(2), 105–108.
Oware, E., Moysey, S. & Khan, T., 2012. Improved imaging of electrically conductive solute plumes using a new strategy for physics-based regularization of resistivity imaging problems, *SEG Technical Program, Expanded Abstracts 2012,* pp. 1–6.
Pride, S., 1994. Governing equations for the coupled electromagnetics and acoustics of porous media, *Phys. Rev. B,* **50**(21), 15 678–15 696.
Revil, A., 2012. Spectral induced polarization of shaly sands: Influence of the electrical double layer, *Water Resour. Res.,* **48,** W02517, doi:10.1029/2011WR011260.
Revil, A., 2013a. Effective conductivity and permittivity of unsaturated porous materials in the frequency range 1 mHz–1 GHz, *Water Resour. Res.,* **49,** doi:10.1029/2012WR012700.
Revil, A., 2013b. On charge accumulations in heterogeneous porous materials under the influence of an electrical field, *Geophysics,* **78**(4), D271–D291.
Revil, A. & Jardani, A., 2010. Seismoelectric response of heavy oil reservoirs. Theory and numerical modelling, *Geophys. J. Int.,* **180,** 781–797.
Revil, A. & Mahardika, H., 2013. Coupled hydromechanical and electromagnetic disturbances in unsaturated porous materials, *Water Resour. Res.,* **49,** 1–23.
Revil, A., Barnier, G., Karaoulis, M., Sava, P. & Jardani, A., 2014. Seismoelectric coupling in unsaturated porous media: theory, petrophysics, and saturation front localization using an electroacoustic approach, *Geophys. J. Int.,* **196**(2), 867–884.
Sava, P. & Revil, A., 2012. Virtual electrode current injection using seismic focusing and seismoelectric conversion, *Geophys. J. Int.,* **191**(3), 1205–1209.
Stern, O., 1924. Zur theorie der electrolytischen Doppelschicht (The theory of the electrolytic double layer), *Zeitschrift für Elektrochemie,* **30,** 508–516.
Vinegar, H.J. & Waxman, M.H., 1984. Induced polarization of shaly sands, *Geophysics,* **49,** 1267–1287.
Wang, H.F., 2000. *Theory of Linear Poroelasticity with Applications to Geomechanics and Hydrogeology, Princeton Series in Geophysics,* 287 pp., Princeton Univ. Press.
West, M.T.N., Butler, K.E. & Barrash, W., 2010. Comparing theoretical and calculated seismoelectric transfer functions at the Boise hydrogeophysical research site, in *GeoCanada 2010 – Working with the Earth, Scientific Meeting.,* Calgary, May 10–13, Extended Abstract, 4 pp.
Zhou, J., Revil, A., Karaoulis, M., Hale, D., Doetsch, J. & Cuttler, S., 2014. Image-guided inversion of electrical resistivity data, *Geophys. J. Int.,* **197,** 292–309.
Zhu, Z. & Toksöz, M.N., 2003. Crosshole seismoelectric measurements in borehole models with fractures, *Geophysics,* **68**(5), 1519–1524.
Zhu, Z. & Toksöz, M.N., 2013. Experimental measurements of streaming potential and seismoelectric conversion in Berea sandstone, *Geophys. Prospect.,* **61,** 688–700.
Zhu, Z., Haartsen, M.W. & Toksöz, M.N., 1999. Experimental studies of electrokinetic conversions in fluid-saturated borehole models, *Geophysics,* **64,** 1349–1356.

APPENDIX A

We discuss below the frequency dependence of the streaming potential coupling coefficient $C = -\hat{Q}_V k/(\eta_f \sigma)$, also addressed by Pride (1994) (with respect to the zeta potential-based model) but also in Appendix A of Revil & Mahardika (2013) and Bolève *et al.* (2007) for the effective-charge type model. In both cases, this frequency dependence is coming from the transition between the viscous to inertial flow domains in the Navier–Stokes equation governing the flow properties at the pore scale. The associated relaxation time τ_k given by (Pride 1994),

$$\tau = \frac{k\rho_w F}{\eta_w}, \tag{A1}$$

where k represents the permeability of the porous material in the viscous-flow domain, F is the formation factor, ρ_w and η_w are the mass density and dynamic viscosity of the pore water. The

Downloaded from http://gji.oxfordjournals.org/ at Colorado School of Mines on June 26, 2014

associated critical frequency is given by $f_c = 2\pi\tau$. Typically, this critical frequency is above 10 kHz (Revil & Mahardika 2013 and references therein).

West *et al.* (2010) reported a frequency dependence of C at the Boise research site at very low frequencies. Jardani *et al.* (2009) reported the values of the streaming potential coupling coefficient at this site as well as the permeability and formation factor. This site is characterized by an unusually coarse material: a bit of sand, a lot of gravels and pebbles. Table 3 in Jardani *et al.* (2009) provides measurements of the parameters entering the critical frequency: $k = 10^{-11}$ m^2, $F = 10$ and $\rho_w = 10^3$ kg m^{-3} $\eta_w = 10^{-3}$ Pa s. This yields $\tau = 10^{-4}$ s or alternatively a critical peak frequency of 1.6 kHz. However, such very coarse materials would be unusual in most field studies and the frequency dependence of the streaming potential coupling coefficient can be therefore safely neglected.

Downloaded from http://gji.oxfordjournals.org/ at Colorado School of Mines on June 26, 2014